Grain Boundary Character Distribution of Nanocrystalline Cu Thin Films Using Stereological Analysis of Transmission Electron Microscope Orientation Maps

A.D. Darbal,[1,†] K.J. Ganesh,[2,‡] X. Liu,[1] S.-B. Lee,[1] J. Ledonne,[1] T. Sun,[2,#] B. Yao,[2,§] A.P. Warren,[3] G.S. Rohrer,[1] A.D. Rollett,[1] P.J. Ferreira,[2] K.R. Coffey,[3] and K. Barmak[1,*]

[1]Materials Research Science and Engineering Center, Carnegie Mellon University, 5000 Forbes Avenue, Pittsburgh, PA 15213, USA
[2]Materials Science and Engineering Program, The University of Texas at Austin, 1 University Station, Austin, TX 78712, USA
[3]Advanced Materials Processing and Analysis Center, University of Central Florida, 4000 Central Florida Boulevard, Orlando, FL 32816, USA

Abstract: Stereological analysis has been coupled with transmission electron microscope (TEM) orientation mapping to investigate the grain boundary character distribution in nanocrystalline copper thin films. The use of the nanosized (<5 nm) beam in the TEM for collecting spot diffraction patterns renders an order of magnitude improvement in spatial resolution compared to the analysis of electron backscatter diffraction patterns in the scanning electron microscope. Electron beam precession is used to reduce dynamical effects and increase the reliability of orientation solutions. The misorientation distribution function shows a strong misorientation texture with a peak at 60°/[111], corresponding to the Σ3 misorientation. The grain boundary plane distribution shows {111} as the most frequently occurring plane, indicating a significant population of coherent twin boundaries. This study demonstrates the use of nanoscale orientation mapping in the TEM to quantify the five-parameter grain boundary distribution in nanocrystalline materials.

Key words: stereology, orientation mapping, grain boundary character distribution, precession microscopy

INTRODUCTION

Crystal orientation imaging using automated analysis of electron backscattered diffraction (EBSD) patterns in the scanning electron microscope (SEM) is well established and widely used (Adams et al., 1993; Dingley, 2004). With automated serial sectioning using focused ion beam milling, one can obtain three-dimensional (3D) orientation data from which it is possible to extract the complete 3D network of grain boundaries (Rohrer et al., 2010b). Alternately, stereological analysis of orientation maps from planar sections can be employed to obtain the average properties of the grain boundary network (Saylor et al., 2004b). Methods such as these have been useful in investigating the crystallography of grain boundaries and the impact of the distribution of grain boundary types on the properties of polycrystalline materials (Rohrer et al., 2004a). However, the use of SEM-EBSD orientation imaging is not reliable for the purpose of investigating grain boundaries in polycrystalline materials where the average grain size is in the 100 nm range. This limitation

is due to the fact that the spatial resolution of SEM-EBSD orientation imaging is limited to tens of nanometers (35 ± 5 in the x direction and 90 ± 15 in the y direction), as determined by Zaefferer (2007), which is not adequate to map the shapes of grain boundaries with lengths smaller than a few hundred nanometers. This provides the motivation for employing the transmission electron microscope (TEM) for large-scale orientation imaging and grain boundary characterization. The use of the TEM provides an order of magnitude improvement in the spatial resolution, thereby making it possible to study polycrystalline materials not possible by SEM-EBSD analysis (Dingley, 2006; Ganesh et al., 2010, 2012; Liu et al., 2011). The objective of this work is to demonstrate the quantitative investigation of grain boundary character distribution in thin Cu films by combining stereological analysis and the use of a <5 nm probe (Ganesh et al., 2010), with the recently developed TEM orientation imaging technique known as ASTAR™ (Rauch & Duft, 2005; Rauch & Dupuy, 2005; Rauch & Veron, 2005; Rouvimov et al., 2008).

ASTAR™ was developed recently for automated orientation determination by fast acquisition of spot diffraction patterns in the TEM. In ASTAR™, a dedicated hardware unit is used for precession and automated scanning of a nanosized quasi-parallel electron beam probe. A high speed external optical camera is then used for rapid acquisition of spot diffraction patterns. The acquired spot patterns are indexed automatically using a template matching algorithm. Significant improvement in the reliability of the orientation maps is achieved with electron beam precession (Rouvimov

et al., 2008). The use of precession reduces the dynamical effects and increases the number of spots in the diffraction pattern (Vincent & Midgley, 1994; Oleynikov et al., 2007; Portillo et al., 2010). The use of rapidly acquired spot patterns and the robust template matching algorithm make ASTAR™ highly suitable for obtaining large datasets of crystal orientations and extracting grain boundary distributions.

In the macroscopic description of grain boundaries, which forms the basis of the stereological analysis used here, a general grain boundary is characterized by five parameters: three parameters to specify the lattice misorientation Δg between the adjoining crystals meeting at the grain boundary and two parameters to specify the inclination of the grain boundary plane normal $\mathbf{n}$. The distribution $\lambda(\Delta g, \mathbf{n})$, known as the grain boundary character distribution, gives the relative area of the boundaries with misorientation Δg and boundary normal $\mathbf{n}$. The grain boundary character distribution is measured in units of multiples of a random distribution (MRD), where values greater than 1 indicate that the grain boundary type occurs more frequently than expected in a random distribution. Apart from the distribution of boundaries in the five-dimensional space, it is also useful to consider the distribution of internal grain surfaces $\lambda(\mathbf{n})$, which gives the distribution of grain boundary planes in the crystal frame of reference, averaged over all misorientations (Rohrer et al., 2004b). $\lambda(\mathbf{n})$ is also measured in units of MRD.

Orientation maps from a planar section can provide four of the five parameters: the three misorientation parameters and one of the two parameters describing the inclination of the boundary plane (Saylor et al., 2004a). It is not possible to determine the exact inclination of the grain boundary plane by only considering orientation data from a plane section. However, the set of possible boundary planes are in the zone of the grain boundary trace. If a large number of indistinguishable misorientations are considered, then the true boundary planes should make a relatively larger fraction in the set of possible boundary planes, and an average estimate of $\lambda(\mathbf{n})$ for this misorientation can be made. This is the basis for the stereological analysis used to make a statistical estimate of the grain boundary character distribution. Stereological analysis has been employed successfully for extracting grain boundary character distribution with the SEM-EBSD orientation maps (Saylor et al., 2004a). In this work, a similar analysis of orientation maps is made in nanocrystalline Cu films using the TEM. In a recent study, grain boundaries in nanoscale Cu interconnects were investigated using orientation mapping from ASTAR™ (Ganesh et al., 2012). However, the study of Ganesh et al. (2012) focused on copper lines, instead of copper films for which the texture is significantly different, and it was based on a grain boundary trace analysis of orientation maps that simply classifies $\Sigma 3$ grain boundaries as incoherent [not terminated by (111) planes] or as possibly being coherent twins. By contrast, the current study analyzes all of the boundaries and provides a stereological

estimate of the relative areas of grain boundary planes with all possible orientations (Saylor et al., 2004a).

To emphasize, the important requirement that needs to be taken into account for the stereological analysis of the grain boundary character distribution is the need for a sufficient number of grain boundary traces within the plane section. The number of traces needed depends on the resolution of the five parameters and the crystal symmetry. For a cubic system with the five parameters resolved with a resolution of 10°, approximately 50,000 grain boundary traces are sufficient (Saylor et al., 2004a). Given the advancements in automation of modern SEM-EBSD systems, this requirement is not difficult to satisfy. However, automated orientation mapping in the TEM is a relatively new development, and acquisition of orientation data at the scale required for this analysis is challenging. Also, it should be noted that stereological analysis assumes that sample has random orientation texture, and if there is a misorientation texture, then the grain boundary character distribution is accurate only for peaks in the misorientation texture, i.e., where there is sufficient information to carry out the analysis.

In the next section, the samples studied and details of the orientation imaging experiments are discussed. A detailed discussion on calibrating the frame of reference for the orientation maps has been included. It may be noted that so far the use of ASTAR™ has been limited to the study of local misorientation texture. Therefore, not much attention has been given to understanding the rotations between the image and the diffraction pattern. However, when one is concerned with absolute orientation, it is important to determine the inertial sample frame of reference with respect to which the orientation is specified. This calibration is crucial for obtaining reliable results from stereological analysis, and the emphasis placed on this aspect here is motivated by the fact that reliable information on interface character can only be obtained if absolute orientations are measured correctly.

MATERIALS AND METHODS

Two SiO_2 encapsulated Cu thin films with Cu layer thicknesses 36.9 and 46.4 nm were used in this study. Details of the thin film deposition and characterization are available in Sun et al. (2008, 2010). Briefly, the two Cu films studied were sputter deposited onto Si (100) substrates having a 150 nm thick layer of thermally grown SiO_2 and cooled to $-40°C$ by contact with a liquid nitrogen cooled Cu plate. The Cu layer was direct current sputtered from 99.9999% pure Cu targets and was encapsulated between an underlayer of 20 nm thick radio frequency sputter deposited SiO_2 and an overlayer of 20 nm sputter deposited SiO_2 to form a SiO_2 (20 nm sputtered)/Cu/SiO_2 (20 nm sputtered)/SiO_2 (150 nm thermal)/Si structure. The Cu thin films were annealed at 600°C for 30 min in Ar + 3% H_2. Plan-view TEM samples were prepared using a back-etching technique by thinning initially with HF + HNO_3 solution and subsequently a diluted HF solution (Yao et al., 2006). The thickness of the Cu

layer was measured using X-ray reflectivity at the Stanford Synchrotron Radiation Lightsource (SSRL; Sun et al., 2010). The thicknesses of the two films are used as labels for the samples studied for the remainder of this work. The average grain sizes for the 36.9 and 46.4 nm thick films are reported to be 81.4 ± 4.5 and 112.6 ± 7.7 nm (Sun et al., 2010). The diameter of the equivalent circle with an area equal to the average grain area was used as the measure for the aforementioned grain size. Hollow cone dark-field images taken at multiple sample tilts in the TEM were used to calculate the grain size (Yao et al., 2010). Twin boundaries were excluded in this grain size calculation.

The orientation imaging microscopy of the two SiO_2-encapsulated Cu films studied was performed on a JEOL 2010F (JEOL Ltd., Tokyo, Japan) field emission gun TEM/scanning TEM (STEM) at an operating voltage of 200 kV. The lens configurations to obtain a probe size less than 5 nm were similar to those employed by Ganesh et al. (2010). Spot diffraction patterns were collected by scanning the beam using a step size of 8 nm over an area containing 180×180 steps. Consistent with the probe size, the step size was chosen to optimize the sampling of orientation data and the acquisition time. Fourteen and 20 scan areas were collected for the 36.9 and 46.4 nm thick films, respectively. A precession angle of 0.4° was used while acquiring all the spot diffraction patterns. The intensity of the forward beam was used to reconstruct a virtual bright-field image in a manner similar to bright-field imaging in STEM mode (Rauch & Dupuy, 2005). Therefore, every pixel in the virtual bright-field image could be associated with a diffraction pattern. The diffraction patterns were collected using the external optical charge-coupled device camera at 25 frames per second at a reduced binning of 150×150 pixels. For automated indexing, 1,326 templates were generated so that the disorientation (minimum misorientation) between two successive templates is approximately 1° (Rauch & Dupuy, 2005).

The orientation images obtained from ASTAR™ were then exported to TexSEM Laboratories Orientation Imaging (TSL OIM™; EDAX, Mahwah, NJ, USA) analysis software for further data processing. The first step in data processing was to use a cleanup procedure to correct spurious points in the orientation map due to incorrect indexing. Diffraction patterns may be incorrectly indexed in cases where the spot intensities are too low or the number of spots is too few. Grain dilation with a minimum grain size of 4 pixels followed by neighbor orientation correlation (level 4) in the TSL OIM™ software was used as the data cleanup procedure. The grain dilation operation was used to ensure that the orientation of the smallest grain is sampled using at least 4 pixels. This is essential to assign reliable orientations for small grains. The neighbor orientation correlation procedure identifies more likely orientations for points in the orientation map that possess a reliability index less than 0.12 (Rauch & Dupuy, 2005). For such points, the orientation is compared with the orientation of the nearest neighbors. If the orientation of at least four of the nearest neighbors is similar to each other and the orientation of the point in con-sideration is different from the orientation of at least four nearest neighbors, then the orientation of the point is changed to the orientation of the four nearest neighbors similar in orientation. Small changes in orientation solutions for points within a grain were commonly observed due to local bending of the thin film. To eliminate these orientation fluctuations, an average orientation was assigned to all points within a grain. After sampling numerous misorientation profiles within grains, it was observed that the maximum misorientation within a grain was 10°. Therefore, for the purpose of assigning a single average grain orientation, two neighboring points with disorientation less than 10° were considered to be part of the same grain. For the specific sequence of clean up steps used in this study, the maximum fraction of points changed due to data clean up was approximately 5%. Grain boundary traces were then extracted with a tolerance of 2 pixels from the cleaned orientation data using the method by Wright and Larsen (2002). Forty-eight thousand and 57,000 boundary traces were extracted for the 36.9 and 46.4 nm thick films, respectively. A representative color-coded inverse pole figure map from the 46.4 nm thick Cu film is shown in Figure 1(left) with the corresponding color code also shown in Figure 1(right). As a useful comparison, the corresponding correlation map is shown in Figure 2. The correlation index for a given pixel in the orientation map gives the degree of correlation between the observed diffraction and the precalculated template (Rauch & Veron, 2005). The image in Figure 2 is shaded such that the bright regions correspond to a high correlation index. Grain boundary traces extracted from the orientation map shown in Figure 1(left) are shown in Figure 3. The choice of parameterization for the description of misorientation and grain boundary normal for stereological analysis is consistent with that used by Saylor et al. (2004a). The misorientation space was parameterized using the Euler angles (ϕ_1, Φ, ϕ_2) (Bunge convention) with 10° discretization (Saylor et al., 2004a). The grain boundary plane normal was parameterized using the two spherical angles θ and φ to specify the inclination of the boundary normal in the crystal frame of reference. For the given choice of parameterization, the resolution of the discretized five-parameter space is approximately 10°.

Frame of Reference Calibration

As mentioned in the Introduction, it is important to calibrate the fixed sample reference frame with respect to which the crystal orientations are specified. This involves two aspects: (a) calibration of the rotation between the image and the diffraction pattern, and (b) knowledge of the sample reference frame with respect to the image. The scanning direction is chosen such that the virtual bright-field image coincides with the TEM bright-field image. In other words, this ensures that no additional rotation is introduced between the image and the diffraction pattern due to the orientation of the scanning direction. Furthermore, it is necessary to calibrate the image rotation with respect to the diffraction pattern for the microscope used for mapping (Williams & Carter, 2009). This standard calibration was performed using
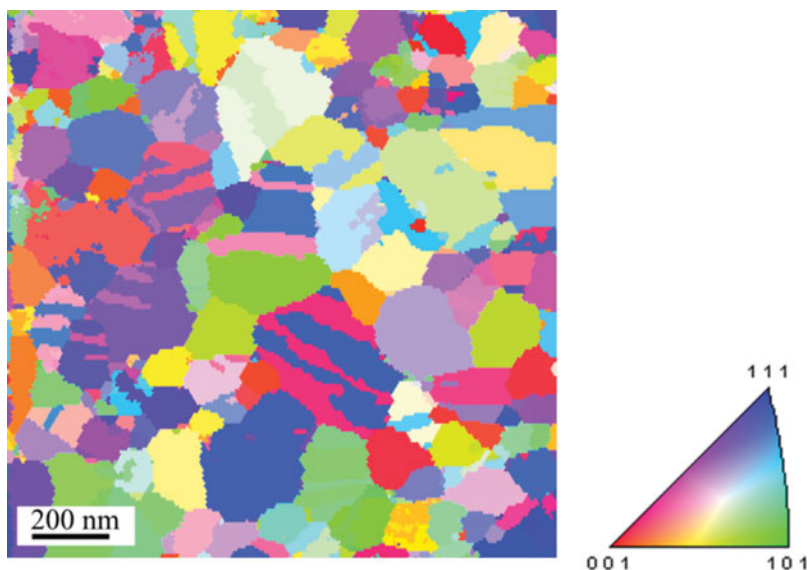
Figure 1. Representative color-coded inverse pole figure map from the 46.4 nm thick Cu film. The color coding for the orientations is shown in the legend.
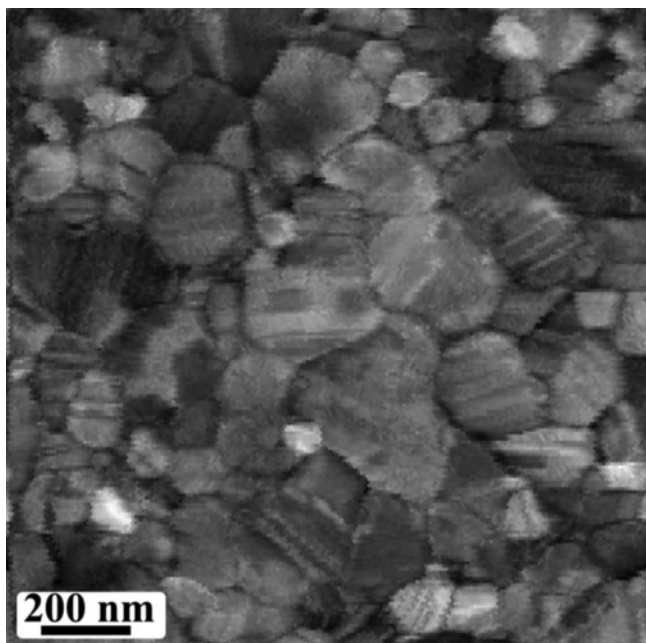
**Figure 2.** Correlation index map corresponding to the orientation map shown in Figure 1.
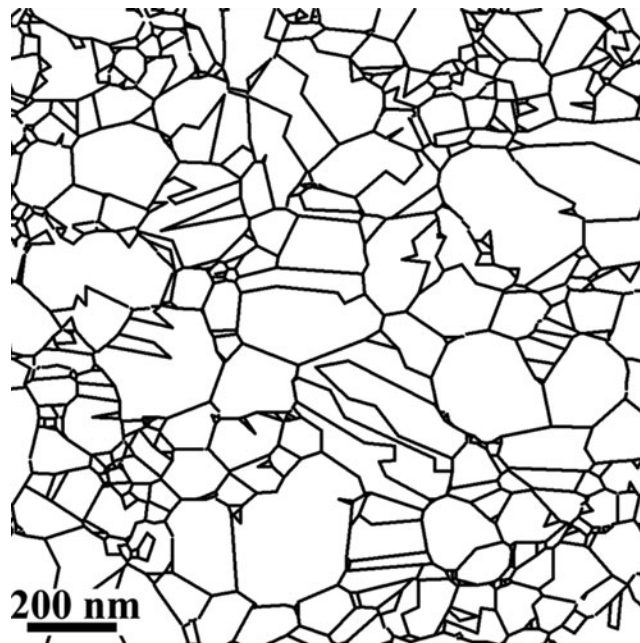
Figure 3. Grain boundary traces extracted from the orientation map shown in Figure 1.

a MoO$_3$ crystal, and it was found that a rotation of 186° in the counter-clockwise direction of the diffraction pattern is needed to make it coincide with the diffraction pattern.

The set of three Bunge Euler angles for each pixel in the orientation map was imported into the TSL OIM™ data analysis software for subsequent analysis. It is important to note that the definition of the Euler reference frame for TSL OIM™ data analysis software is not consistent with ASTAR™ as seen in Figure 4. According to the notation used in TSL OIM™ data analysis, the x axis is denoted as the rolling direction (RD), the y axis is denoted as the transverse direction (TD), and the z axis is denoted as the

normal direction (ND) (Dingley, 2004). Figure 4 shows that there is a net 90° rotation between the reference systems. The 111 pole figure from a point in the orientation map from a Cu thin film in the frame of reference used in ASTAR™ is shown in Figure 4a. The 111 pole figure from the same point plotted using the TSL OIM™ data analysis software is shown in Figure 4b. The difference in the two pole figures is due to the fact that definitions of the reference systems for TSL OIM™ data analysis and ASTAR™ are different. This needs to be taken into account when the data from ASTAR™ are exported to TSL OIM™ data analysis. Therefore, the orientation data were rotated by
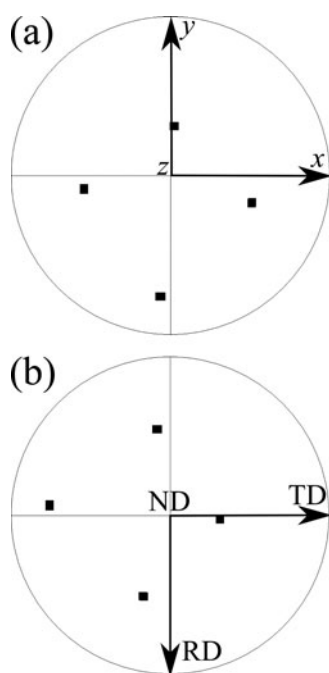
**Figure 4.** An example of a 111 pole figure in (**a**) the ASTAR^{TM} frame of reference and (**b**) the TSL OIM^{TM} frame of reference. For the latter, x is designated the rolling direction (RD) and y the transverse direction (TD). The direction normal to the plane of the page is z or ND. The orientation data in TSL OIM^{TM} data analysis software should be given a $+90°$ counter-clockwise active rotation about the normal direction (z) to account for the difference in the ASTAR^{TM} and TSL OIM^{TM} frames of reference.

$+90°$ in the counter-clockwise direction about the ND using TSL OIM^{TM} data analysis software. It may be noted that a 90° rotation can also be applied to the data using ASTAR^{TM} before exporting it.

RESULTS

The orientation distribution (OD) from the combined data taken from the 36.9 and 46.4 nm thick Cu films is shown in Figure 5 as an inverse pole plot. The OD for both the Cu films analyzed was similar, and hence only combined data are shown to have improved counting statistics. The OD shows a weak orientation texture with the frequency of [111] poles perpendicular to the sample surface as 2.1 MRD. The presence of this relatively low level of orientation bias does not have a significant impact on the grain boundary character distribution determined from stereological analysis (Saylor et al., 2004b).

The misorientation distribution (MD) is shown in Figure 6. The axis-angle convention is used to denote the misorientation. Figure 6 shows a prominent peak at 60°/ [111] misorientation with a frequency of 19.2 MRD. This misorientation is commonly referred to as the Σ3 misorientation in coincident site lattice convention (Bollmann, 1970; Randle, 1996). The boundary plane distribution $\lambda(\mathbf{n}/\Delta g)$ for the Σ3 misorientation is shown as a stereographic projection in Figure 7; $\lambda(\mathbf{n}/\Delta g)$ shows a peak of 500 MRD and
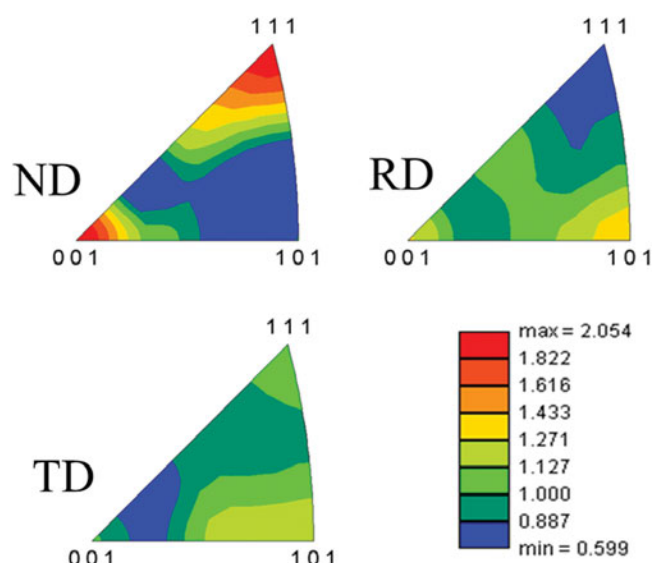

Figure 5. Inverse pole plots from the combined orientation data for the 36.9 and 46.4 nm thick Cu films. Intensity is given in units of MRD. A weak {111} fiber texture may be noted.

800 MRD at the (111) position for the 36.9 nm and 46.4 nm thick Cu films, respectively. This peak corresponds to a coherent twin boundary (the coherent Σ3). The distribution of grain boundary plane normals averaged over all grain boundary misorientations is shown in Figure 8. The distribution of the boundary plane normals is relatively isotropic with a clear preference for the {111} planes.

DISCUSSION

Earlier experimental and theoretical studies of the distribution of grain boundaries show that grain boundaries with low energies have high populations (Saylor et al., 2004b; Rohrer et al., 2004a, 2004b). As mentioned earlier, the peak in the grain boundary character distribution in Figure 7 corresponds to a coherent twin boundary. It is well known that the energy of a coherent twin boundary is significantly lower compared to other boundaries and that coherent twin boundaries are observed frequently in Cu (Randle et al., 2008; Lu et al., 2009). Therefore, the peak at the (111) pole is consistent with these observations. It is also interesting to compare the distribution of grain boundary planes averaged over all misorientations, which shows that {111} planes occur most frequently. This is consistent with the calculated surface energy using the broken bond model for face-centered cubic (fcc) crystals (Mackenzie et al., 1962; Rohrer et al., 2004a, 2004b), according to which the {111} planes in the fcc crystal have the lowest surface energy. Studies of the grain boundary distribution and grain boundary energy anisotropy in fcc Al and Ni using experimental measurements and calculated energies show similar trends between the surface energy and the frequency of grain boundary planes (Li et al., 2009; Rohrer et al., 2010a; Holm et al., 2011). A similar trend between the frequent occurrence of low energy planes along the interfaces between adjoining
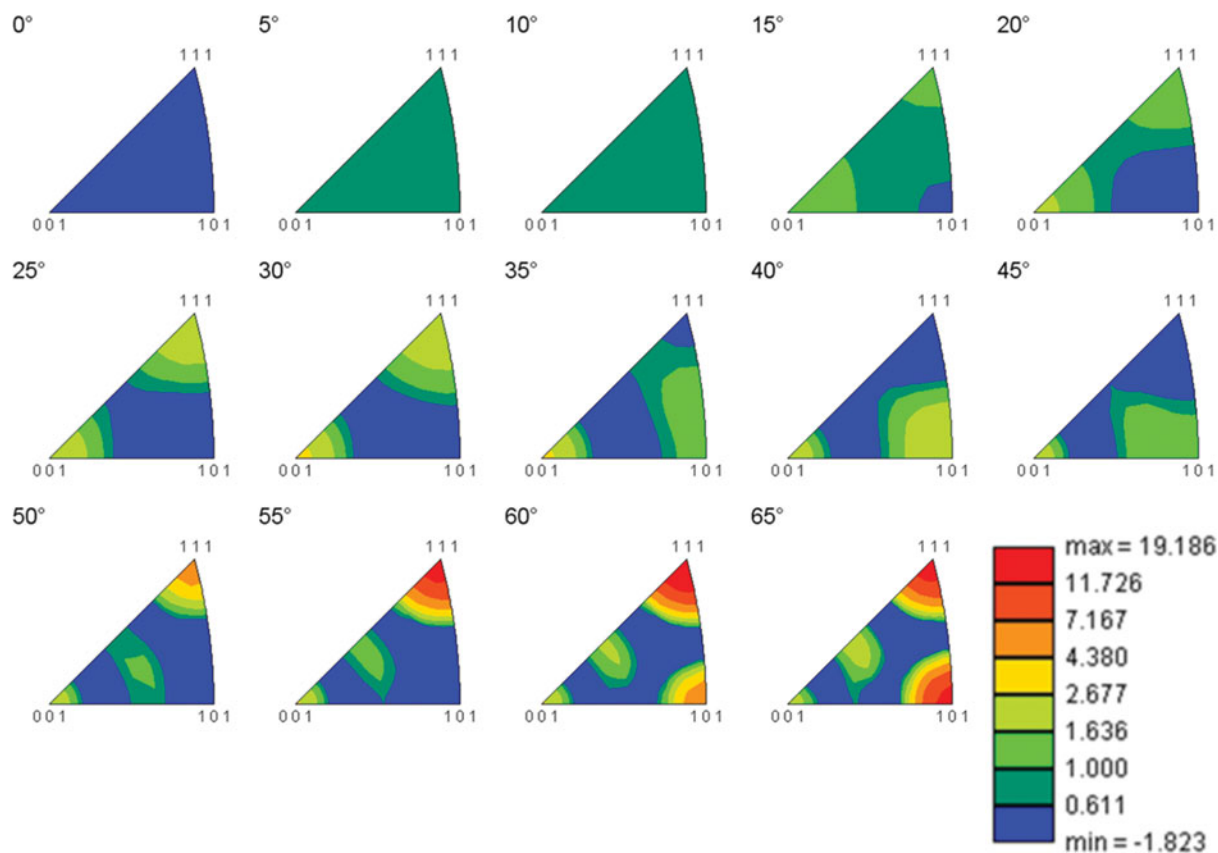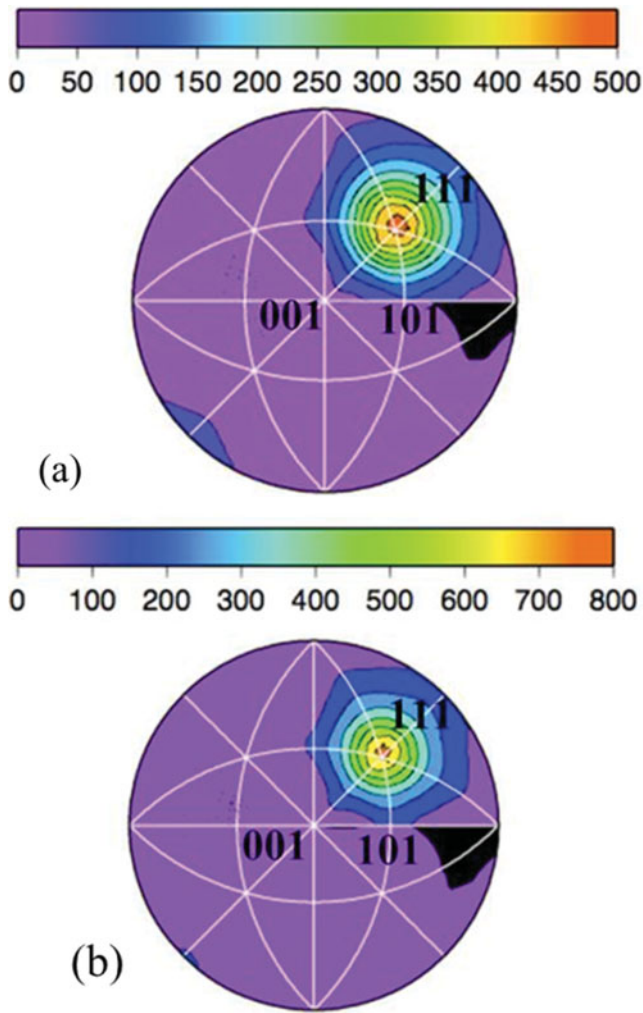
Figure 6. Misorientation distribution from the combined orientation data for the 36.9 and 46.4 nm thick Cu films with intensity in units of MRD. A strong peak at the Σ3 misorientation can be observed.

crystals has been observed in other systems such as MgO, SrTiO$_3$, MgAl$_2$O$_4$, and TiO$_2$ (Saylor et al., 2004c and references therein).

As mentioned earlier, the misorientation distribution in Figure 6 shows a high density of Σ3 or twin boundaries. Given their frequent occurrence, it is interesting to further investigate whether the twin boundaries are coherent or incoherent. Twin boundaries are considered coherent when the boundary plane is {111} and are considered incoherent otherwise. It is well known that the properties of twin boundaries significantly depend on whether they are coherent or incoherent (Olmsted et al., 2009). This is of particular interest in the study of classical resistivity size effect in Cu resistivity increase due to incoherent twin boundaries is significantly higher than that of coherent twin boundaries (Lu et al., 2004; Feldman et al., 2010). The grain boundary character distribution in Figure 7 shows a significant occurrence of boundary planes that are not exactly {111}, thus indicating the presence of incoherent boundaries.

To gain a more quantitative measure of the fraction of incoherent boundaries, trace analysis was used. In trace analysis, to determine whether a twin boundary is coherent, the trace of the boundary plane is matched with the trace of the {111} (Wright & Larsen, 2002). If the two traces are within a predefined tolerance, then the twin boundary is considered to be coherent. However, it should be noted that the matching between the trace of the boundary plane and

the {111} is only a necessary, but not a sufficient, condition for a twin boundary to be coherent. This is because the trace of the boundary plane matches the trace of all the planes whose normals are perpendicular to the boundary line segment. Therefore, when a boundary is classified as a coherent boundary, it is ambiguous, and the true fraction of coherent twin boundaries is always less than or equal to the estimate from trace analysis. Figure 9 shows the grain boundary traces extracted using the orientation map for the 46.4 nm thick Cu film with the coherent and the incoherent twin boundaries identified using trace analysis. It was found that 45% of the Σ3 boundaries are coherent twins. This is an interesting observation, as earlier investigations of nanocrystalline Cu assumed all the twin boundaries to be coherent due to the lack of a suitable technique to investigate grain boundaries at this scale (Lu et al., 2004; Sun et al., 2010). Clearly, this assumption is not valid and further investigation in this regard may be necessary. It is interesting to compare the percentage of coherent Σ3 boundaries observed in this study (45%) with earlier investigations of twin boundaries in Cu interconnect lines using trace analysis of EBSD orientation maps (Wright & Larsen, 2002). It was found that 62% of the Σ3 boundaries in these Cu interconnect were coherent. The grain size of Cu studied by Wright and Larsen was in the 2–3 μm range, thus making it amenable for EBSD measurements. In this regard, it is also interesting to discuss the study on five parameter grain
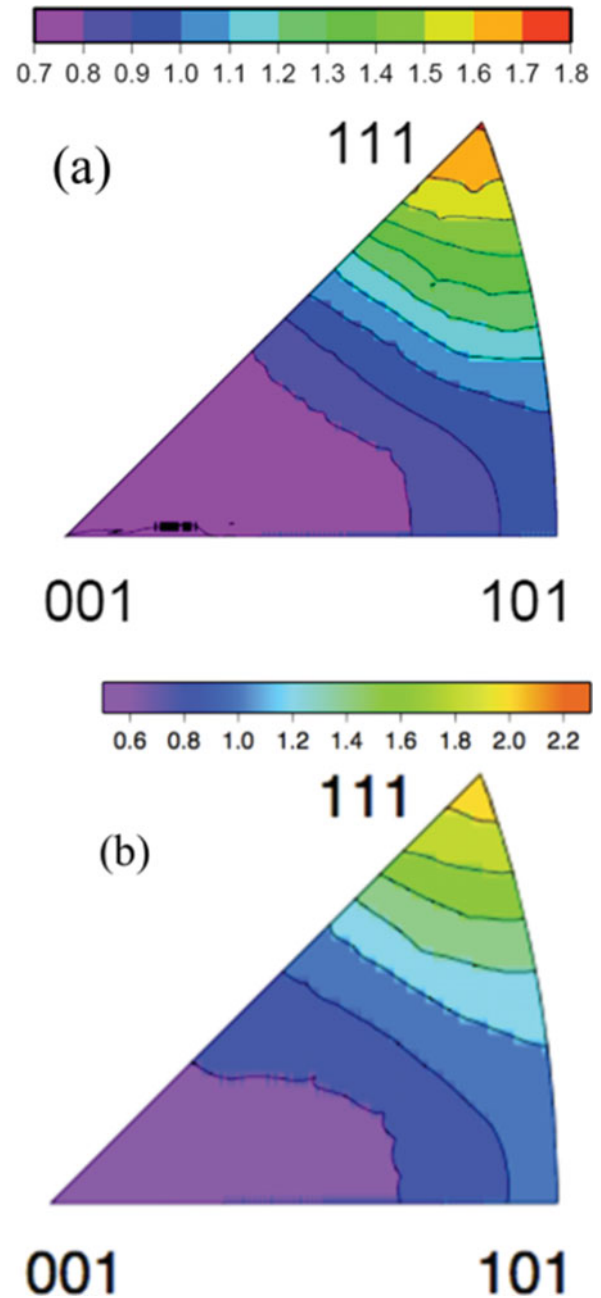
Figure 7. The distribution of grain boundary planes on a [001] stereographic projection for the Σ3, i.e., 60°/[111], misorientation for (a) 36.9 nm and (b) 46.4 nm thick Cu films. The intensity is expressed in units of MRD. For both samples a peak is found at the [111] pole, which corresponds to a coherent Σ3 twin boundary.

boundary characterization on grain boundary engineered (GBE) bulk Cu (Randle et al., 2008) with grain sizes in the tens of micrometer range. They observed that the fraction of Σ3 boundaries increased in GBE Cu while the fractional area of {111} remained constant; therefore, a high fraction of incoherent twin boundaries had formed during the thermomechanical treatments associated with GBE. Such differences in the fraction of coherent twin boundaries among bulk, micrometric, and nanometric Cu samples are likely a consequence of the differences in processing methods, i.e., bulk thermomechanical, electroplating, and sputter deposition used for the three types of samples, respectively.

SUMMARY

The use of TEM-based orientation imaging for quantitative investigation of grain boundary characterization in nanocrystalline Cu thin films has been demonstrated. It has been shown here that orientation imaging in TEM is capable of

Figure 8. The distribution of grain boundary planes in the crystal frame of reference $\lambda(\mathbf{n})$ averaged over all misorientations for (**a**) 36.9 nm and (**b**) 46.4 nm thick Cu films. Intensity of the distribution is expressed in units of MRD.

providing large orientation datasets so that statistical methods such as the stereological analysis used in this study can be used. For this purpose, we have employed a stereological analysis on large orientation datasets acquired using the TEM. This means that the quantitative investigation of microstructure in polycrystalline materials is no longer limited by the resolution of SEM-EBSD techniques. However, due care must be taken to understand the effects of lens rotation and the frame of reference used to represent the orientation.

The nanocrystalline Cu films studied in this work show weak ⟨111⟩ fiber texture but a strong Σ3, i.e., [111]/60°,
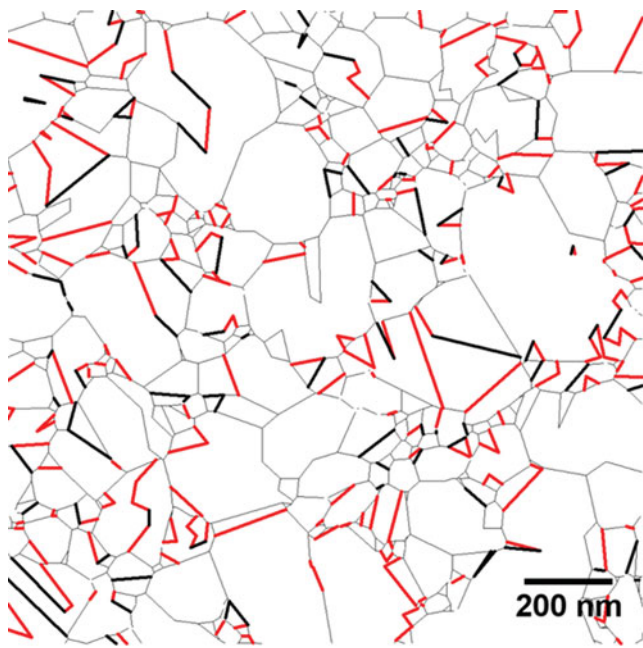
Figure 9. Grain boundary traces extracted from the orientation map for the 46.4 nm thick Cu film with coherent and incoherent twin boundaries identified using trace analysis. Thick red lines correspond to incoherent twin boundaries and thick black lines correspond to coherent twin boundaries. Thin black lines correspond to all other boundaries.

misorientation texture. The distribution of grain boundary planes for this misorientation shows a prominent peak at [111], which shows a high density of coherent twin boundaries. However, it was also found that a significant fraction of the $\Sigma 3$ boundaries are not coherent twin boundaries.

Acknowledgments

References

Adams, B.L., Wright, S.I. & Kunze, K. (1993). Orientation imaging: The emergence of a new microscopy. *Metal Trans A* **24**, 819–831.

Bollmann, W. (1970). *Crystal Defects and Crystalline Interfaces*. New York: Springer Verlag.

Dingley, D. (2004). Progressive steps in the development of electron backscatter diffraction and orientation imaging microscopy. *J Microsc* **213**, 214–224.

Dingley, D.J. (2006). Orientation imaging microscopy for the transmission electron microscope. *Microchimica Acta* **155**, 19–29.

Feldman, B., Park, S., Haverty, M., Shankar, S. & Dunham, S.T. (2010). Simulation of grain boundary effects on electronic transport in metals, and detailed causes of scattering. *Phys Staus Solidi B* **247**, 1791–1796.

Ganesh, K.J., Darbal, A., Rajasekhara, S., Rohrer, G.S., Barmak, K. & Ferreira, P.J. (2012). Effect of downscaling copper interconnects on the microstructure revealed by high resolution TEM-orientation-mapping. *Nanotechnology* **23** 135702.

Ganesh, K.J., Kawasaki, M., Zhou, J.P. & Ferreira, P.J. (2010). D-STEM: A parallel electron diffraction technique applied to nanomaterials. *Microsc Microanal* **16**, 614–621.

Holm, E.A., Rohrer, G.S., Foiles, S.M., Rollett, A.D., Miller, H.M. & Olmsted, D.L. (2011). Validating computed grain boundary energies in fcc metals using the grain boundary character distribution. *Acta Mater* **59**, 5250–5256.

Li, J., Dillon, S.J. & Rohrer, G.S. (2009). Relative grain boundary area and energy distributions in nickel. *Acta Mater* **57**, 4304–4311.

Liu, H.H., Schmidt, S., Poulsen, H.F., Godfrey, A., Liu, Z.Q., Sharon, J.A. & Huang, X. (2011). Three-dimensional orientation mapping in the transmission electron microscope. *Science* **332**, 833–834.

Lu, K., Lu, L. & Suresh, S. (2009). Strengthening materials by engineering coherent internal boundaries at the nanoscale. *Science* **324**, 349–352.

Lu, L., Shen, Y., Chen, X., Qian, L. & Lu, K. (2004). Ultrahigh strength and high electrical conductivity in copper. *Science* **304**, 422–426.

Mackenzie, J.K., Moore, A.J.W. & Nichols, J.F. (1962). Bonds broken at atomically flat crystal surfaces—I: Face-centred and body-centred cubic crystals. *J Phys Chem Solids* **23**, 185–193.

Oleynikov, P., Hovmuller, S. & Zou, X.D. (2007). Precession electron diffraction: Observed and calculated intensities. *Ultramicroscopy* **107**, 523–533.

Olmsted, D.L., Foiles, S.M. & Holm, E.A. (2009). Survey of computed grain boundary properties in face-centered cubic metals: I. Grain boundary energy. *Acta Mater* **57**, 3694–3703.

Portillo, J., Rauch, E.F., Nicolopoulos, S., Gemmi, M. & Bultreys, D. (2010). Precession electron diffraction assisted orientation mapping in the transmission electron microscope. *Mater Sci Forum* **644**, 1–7.

Randle, V. (1996). *The Role of Coincident Site Lattice in Grain Boundary Engineering*. London: Cambridge University Press.

Randle, V., Rohrer, G.S., Miller, H.M., Coleman, M. & Owen, G.T. (2008). Five-parameter grain boundary distribution of commercially grain boundary engineered nickel and copper. *Acta Mater* **56**, 2363–2373.

Rauch, E.F. & Duft, A. (2005). Orientation maps derived from TEM diffraction patterns collected with an external CCD camera. *Mater Sci Forum* **495–497**, 197–202.

Rauch, E.F. & Dupuy, L. (2005). Rapid diffraction patterns identification through template matching. *Arch Metall Mater* **50**, 87–89.

Rauch, E.F. & Veron, M. (2005). Coupled microstructural observations and local texture measurements with an automated crystallographic orientation mapping tool attached to a tem. *Materialwiss Werkst* **36**, 552–556.

Rohrer, G.S., El Dasher, B.S., Miller, H.M., Rollett, A.D. & Saylor, D.M. (2004*a*). Distribution of grain boundary planes at coincident site lattice misorientations. *Mat Res Soc Symp Proc* **819**, N7.2.

Rohrer, G.S., Holm, E.A., Rollett, A.D., Foiles, S.M., Li, J. & Olmsted, D.L. (2010*a*). Comparing calculated and mea-

sured grain boundary energies in nickel. *Acta Mater* **58**, 5063–5069.

ROHRER, G.S., LI, J., LEE, S., ROLLETT, A.D., GROEBER, M. & UCHIC, M.D. (2010*b*). Deriving grain boundary character distributions and relative grain boundary energies from three-dimensional EBSD data. *Mater Sci Technol* **26**, 661–669.

ROHRER, G.S., SAYLOR, D.M., DASHER, B.E., ADAMS, B.L., ROLLETT, A.D. & WYNBLATT, P. (2004*b*). The distribution of internal interfaces in polycrystals. *Z Metallk* **95**, 197–214.

ROUVIMOV, S., MOECK, P., RAUCH, E.F., MANIETTE, Y. & BULTREYS, D. (2008). Crystallographic characterization of polycrystalline materials: High resolution automated crystallite orientation. *Microsc Microanal* **14**, 768–769.

SAYLOR, D.M., DASHER, B.S., ADAMS, B.L. & ROHRER, G.S. (2004*a*). Measuring the five-parameter grain-boundary distribution from observations of planar sections. *Metal Mater Trans A* **35**, 1981–1989.

SAYLOR, D.M., DASHER, B.S.E., ROLLETT, A.D. & ROHRER, G.S. (2004*b*). Distribution of grain boundaries in aluminium as a function of five macroscopic parameters. *Acta Mater* **52**, 3649–3655.

SAYLOR, D.M., EL, D.B., PANG, Y., MILLER, H.M., WYNBLATT, P., ROLLETT, A.D. & ROHRER, G.S. (2004*c*). Habits of grains in dense polycrystalline solids. *J Am Ceram Soc* **87**, 724–726.

SUN, T., YAO, B., WARREN, A.P., BARMAK, K., TONEY, M.F., PEALE, R.E. & COFFEY, K.R. (2010). Surface and grain-boundary scattering in nanometric Cu films. *Phys Rev B* **81**.

SUN, T., YAO, B., WARREN, A.P., KUMAR, V., ROBERTS, S., BARMAK, K. & COFFEY, K.R. (2008). Classical size effect in oxide-encapsulated Cu thin films: Impact of grain boundaries versus surfaces on resistivity. *J Vac Sci Technol A* **26**, 605–609.

VINCENT, R. & MIDGLEY, P.A. (1994). Double conical beam-rocking system for measurement of integrated electron diffraction intensities. *Ultramicroscopy* **53**, 271–282.

WILLIAMS, D.B. & CARTER, C.B. (2009). *Transmission Electron Microscopy: A Textbook for Materials Science*, pp. 167–168. New York: Springer.

WRIGHT, S.I. & LARSEN, R.J. (2002). Extracting twins from orientation imaging microscopy scan data. *J Microsc* **205**, 245–252.

YAO, B., PETROVA, R.V., VANFLEET, R.R. & COFFEY, K.R. (2006). A modified back-etch method for preparation of plan-view high-resolution transmission electron microscopy samples. *J Electron Microsc* **57**, 47–52.

YAO, B., SUN, T., WARREN, A., HEINRICH, H., BARMAK, K. & COFFEY, K.R. (2010). High contrast hollow-cone dark field transmission electron microscopy for nanocrystalline grain size quantification. *Micron* **41**, 177–182.

ZAEFFERER, S. (2007). On the formation mechanisms, spatial resolution and intensity of backscatter Kikuchi patterns. *Ultramicroscopy* **107**, 254–266.